GEST: Accurate global ocean surface current reconstruction with multi-scale dynamics-informed neural network

Linyao Ge[1], Guiyu Wang[1], Baoxiang Huang[2,3], Chuanchuan Cao[1], Xiaoyan Chen[1], and Ge Chen[1,3]

[1]Frontiers Science Center for Deep Ocean Multispheres and Earth System, School of Marine Technology, Ocean University of China, Qingdao, China
[2]Department of Computer Science and Technology, College of Computer Science and Technology, Qingdao University, Qingdao, China
[3]Laboratory for Regional Oceanography and Numerical Modeling, Qingdao Marine Science and Technology Center, Qingdao, 266100, China

Correspondence: Baoxiang Huang (baoxianghuang@qdu.edu.cn) and Ge Chen (gechen@ouc.edu.cn)

Abstract. Exceptional precision and excellent resolution reconstruction of sea surface currents are beneficial for exploring complex oceanic dynamic processes. Normally, this required physical inversion models for global or regional oceans are constructed to reconstruct oceanic currents. These models are based on the analysis of sea surface geostrophic and Ekman currents derived from satellite observations of sea level and wind stress fields. Nevertheless, the presence of various typical dynamic processes in marine environments, such as mesoscale eddies and small-scale waves, continues to pose challenges in accurately reconstructing oceanic currents. Meanwhile, any product of surface current that neglects the contribution of wave motion would, at best, be incomplete. Therefore, in this paper, we introduce an accurate sea surface current product at a depth of 15 m, named GEST (Geostrophic-Ekman-Stokes-Tide). This product is produced by a multi-scale dynamics-informed neural network that learns the intricate representation of concealed characteristics in Ekman, geostrophic currents, wave-induced Stokes drift, and TPXO9 tidal currents. Its structure design is predicated upon the intricate coupling relationships between various ocean surface components and the veritable currents discerned by the deployment of drift buoys, with each ocean surface component correlating to discrete physical processes. Compared with the prevailing product, the GEST confers an elevation in precision by approximately 9.2 cm/s over the traditional multinomial fitting method, 10.4 cm/s beyond the OSCAR, and 8.81 cm/s surpassing GlobCurrent.

1 Introduction

The ocean surface currents are quintessential for climatological research and are intricately linked with a plethora of oceanographic applications (Lagerloef et al., 2003; Caniaux et al., 2005; Jin et al., 2014). Granular insights into these currents exert a profound impact on fisheries management, maritime navigation, and marine rescue operations (Lo and McCord, 1998). Specifically, the comprehension of the velocities and directions of ocean surface currents is indispensable for monitoring suspended

---

First Author and Second Author contribute equally to this work

material such as spilled oil, algae, sea ice, and pelagic microplastic (Choi et al., 2013; Yang et al., 2014; Weisberg et al., 2019; Onink et al., 2019), thereby facilitating the efficacious exploration of planktonic ecosystems and the preservation of marine biodiversity (Wahl et al., 1996; Garçon et al., 2001). Therefore, a high-resolution, long-time series ocean surface current is imperative for augmenting extant oceanographic datasets, deepening the understanding of refined ocean dynamical processes
25   and enhancing the precision of prognostications regarding climatic system alterations Chapman and Charantonis (2017).

Cutting-edge technologies have been efficaciously applied to the observation of ocean surface currents. Notwithstanding, a global current observation system that obtains sea surface velocities across the entirety of spatial and temporal dimensions has not been actualized. Despite the manifest success of the Global Drifter Program (GDP) initiated by the National Oceanic and Atmospheric Administration (NOAA) which has run for about 40 years, there are still extant limitations and shortcomings,
30   such as the granularity of space-time sampling and the scarcity of coastal distributions.

It is widely acknowledged that algorithms derived from satellite data can account for approximately 70% of the dynamics of global ocean currents (Sudre and Morrow, 2008), within which the large-scale geostrophic circulation has been ascertained for the past 25-30 years. In establishing a stable equilibrium between wind-induced friction stresses and Coriolis forces, the Elman current serves as a fundamental theoretical framework for comprehending the wind-driven aspects of oceanic circulation and
35   is likewise recognized as a principal dynamic mechanism in ocean currents (Ekman, 1905). Furthermore, high-resolution Sea Surface Temperature (SST) products and Ocean Color (OC) images have significantly enhanced the accuracy of reconstructed ocean currents models by employing methodologies derived from the Maximum Cross-Correlation technique and surface quasi-geostrophic theory (Bowen et al., 2002; González-Haro and Isern-Fontanet, 2014; Liu et al., 2017; Rio and Santoleri, 2018). The construction of global physical estimation models, such as OSCAR (Ocean Surface Current Analysis Real Time),
40   GEKCO (Geostrophic and Ekman Current Observatory), and the GlobCurrent project (Bonjean and Lagerloef, 2002; Dohan and Maximenko, 2010; Sudre et al., 2013; Rio et al., 2014), represents a remarkable advancement in the estimation of long-time series ocean surface current datasets. Wind-driven currents were obtained by Sudre et al. (2013) through the reanalysis of wind stress fields using a bi-parameter model, with parameters adjusted using linear stability equations informed by the assimilation of drifter data. Rio et al. (2014) utilized a new $0.25°$ CNES-CLS13 MDT by assimilating drifter observations, leading to an
45   average increase of 200% in geostrophic velocities in strong currents. Additionally, an empirical Ekman model encompassing two levels (0 m and 15 m) was calculated using surface drifters and Argo floats. Both algorithms contribute to enhancing the accuracy of ocean current estimations. Bonjean and Lagerloef (2002) improved the estimation of tropical circulation based on quasi-linear and steady physics by combining geostrophic, Ekman, and Stommel shear dynamics, and a complementary term from surface buoyancy gradient. All these surface currents were directly calculated from geostrophic and wind-induced
50   Ekman currents. In physical ocean environment, however, the movement of upper oceans layers is attributed to a variety of environmental factors and can be categorically divided into four main types: large-scale ocean circulations, mesoscale eddies, submesoscale dynamics, and small-scale phenomena such as internal waves and storm surges. Wave-induced transport acts either as an enhancement or attenuation to the mean flow within the Ekman layer and should also be regarded as an essential source of the ocean current (Bi et al., 2012).

55   The aforementioned methodology of developing a mathematical model for ocean currents based on oceanographic physical mechanisms can be classified as a model-driven approach. As the scale of data expands, data-driven methods, particularly deep learning, are increasingly utilized to dramatically improve the state-of-the-art in liquid computing (Guan et al., 2022), atmosphere forecasting (Lam et al., 2023; Bi et al., 2023), and oceanography predicting (Ge et al., 2023). Deep learning allows computational models that are composed of multiple processing layers, enabling the learning of data representations with varied

60   levels of abstraction (LeCun et al., 2015). The designation of these models significantly influences their learning capabilities, as various data sources offer distinct data representations. Convolution neural networks, which exhibit superior performance in computer vision, rely on their architecture specifically designed for translation invariance (He et al., 2016; Liu et al., 2022). Similarly, natural language processing models, including long short-term memory (Hochreiter and Schmidhuber, 1997) and the Transformer model (Vaswani et al., 2017), are equipped with specialized mechanisms to memorize characteristics that evolve

65   over time and to capture the intricate relationships among different vocabulary elements. Consequently, to achieve the accurate reconstruction of global ocean surface currents, a neural network architecture specifically tailored for this purpose is essential.

In this paper, we develop a multi-scale dynamics-informed neural network based on the inherent coupling relationship between drifter observations and the velocities of ocean surface current components such as geostrophic and Ekman currents, wave-induced tidal currents, and Stokes drift. This approach leads to a highly accurate ocean surface current product, integrat-

70   ing multi-scale dynamical processes. This global daily product covers the period of 2006-2019, with a 0.25° spatial resolution, and is compared with the OSCAR product and the GlobCurrent project products.

The organization of the remaining parts of this paper is as follows. Section 2 is concerned with the data used to calculate the components of the currents. Section 3 presents the analysis of the coupling relationship between multi-scale dynamic processes for reconstructing ocean surface currents. Section 4 describes the structure of the multi-scale dynamics-informed

75   neural network. Section 5 shows the results of flow field estimates and provides a discussion of our estimation work. Finally, we reveal the conclusions in Sect. 6

2   Data

2.1   Tidal data

Recently, numerous tidal estimation models with varying resolutions and precision have emerged due to the inadequacy of tidal

80   observation stations (e.g., HAMTIDE, FES, and TPXO) (Lyard et al., 2006; Taguchi et al., 2014). In our study, we utilized tidal data from the latest version of TPXO models available at the time, namely the TPXO9 model. This model is founded on the two-dimensional positive pressure fluid equation, leveraging the generalized inversion method to assimilate altimetry data (e.g., satellite altimetry from T/P, ERS1, 2, Envisat satellites) and in situ station-based tidal data. Subsequently, the data is fitted using the least squares (LS) method (Egbert and Erofeeva, 2002). The TPXO9 model, curated by Gary Egbert and Lanna

85   Erofeeva from Oregon State University, USA, and utilized in our research for the global hourly tidal dataset, is renowned for its accuracy and reliability. It boasts a low root mean square error of M2 constituents across various oceanic regions, including

the deep ocean, shallow seas, and continental shelf (Sun et al., 2022). The derived tidal data exhibits a resolution of $1/6°$ and encompasses harmonic constants of 15 constituents, comprising eight major ones (M2, S2, N2, K2, K1, O1, P1, and Q1).

2.2 Wind data

90   The global daily wind fields utilized in our study were obtained from the QuikSCAT and Windsat satellites, launched by the United States and operational in orbit. These wind fields exhibit a spatial resolution of $0.25° \times 0.25°$ and cover a time span of 14 years from January 2006 to January 2019. Subsequently, this dataset was employed to compute wind stress fields using a bulk formula, incorporating a drag coefficient (Cd) derived from a curve-fitting procedure that combines data for low-to-moderate winds with data for high wind speeds (Oey et al., 2006).

95   Based on reanalyzed wind stress fields, our aim is to extract wind-induced Ekman currents. These currents exhibit a perpendicular orientation to the direction of wind stress and are shifted to the left in the Southern Hemisphere (and conversely in the Northern Hemisphere), resulting in a spiral motion due to the influence of turbulent viscosity, which is contingent upon the local oceanic state (Roach et al., 2015).

2.3 Copernicus marine service global geostrophic currents and Stokes drift

100   This paper utilizes reanalyzed daily geostrophic velocities provided by the Copernicus Marine Service, featuring a spatial resolution of $0.25° \times 0.25°$ and spanning the years 2006 to 2019 (Pujol et al., 2016). For latitudes beyond $\pm5°$ N, geostrophic currents are derived from altimeter maps of the Absolute Dynamic Topography (ADT) using a nine-point stencil width methodology. However, in proximity to the equatorial zone, where the geostrophic balance becomes inapplicable, a β-plane approximation introduced by Lagerloef et al. (1999) is adopted.

105   Additionally, the Stokes drift data are sourced from the Global Ocean Waves Reanalysis (WAVERYS) numerical assimilation products covering the period from 2006 to 2019, provided by the Copernicus Marine Service. These products feature grid points with a spatial resolution of $0.2°$ longitude and $0.2°$ latitude spacing. The dataset comprises 3-hour instantaneous fields of integrated wave parameters, such as Sea Surface Wave Significant Height (SWH), Sea Surface Wind Wave Direction (WW), and Stokes Drift Velocities (VSDXY). They are derived from the global wave reanalysis conducted using the

110 MeteoFranceWAve-Model (MFWAM) wave model, which assimilates altimeter wave data and directional spectrum information provided by Sentinel-1 (Law-Chune et al., 2021).

2.4 Surface drifting buoys

AOML's Global Drift Program comprises a worldwide network of over 1,000 satellite-tracked surface drifting buoys ("drifters"), which collect extensive surface velocity measurements and track current directions using the Lagrangian method. In this inves-

115 tigation, we utilize the velocities from these in situ drifters as "reference tags." This comprehensive global dataset, featuring long time series, is interpolated at hourly intervals, providing detailed insights into global high-frequency and small-scale oceanic processes. Positions and velocities are determined by locally modeling the trajectory as first-order polynomials, with

coefficients obtained through the maximization of the likelihood function (Elipot et al., 2016, 2022). To illustrate the distribution of collocated drifter data, the global spatial distribution of drifter observations per $1° \times 1°$ cell is depicted in Fig.,1.
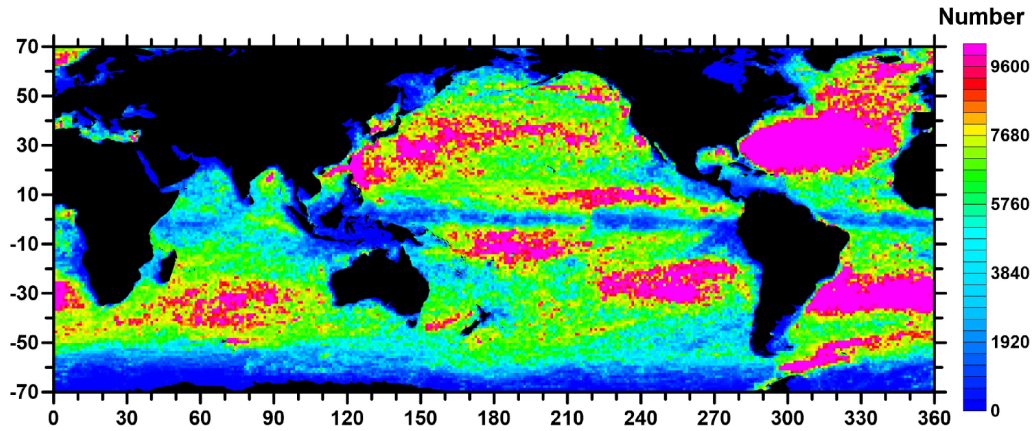
Figure 1. Spatial distribution for the drifter observations per $1° \times 1°$ from 1999 to 2019.

3 Multiscale dynamics for current reconstruction

Designing an accurate and impactful neural network model requires careful consideration of the dynamics and knowledge of current reconstruction. This involves transferring the dynamics interaction into the model structure and adopting a suitable neural operator. Therefore, the initial step involves exploring the global correlation distribution of various currents with drifters and understanding their dynamic interactions with the physical environment, which contains the local applicability of wind-driven currents, decay scales of Stokes drift and tidal currents, and coupling effect between different currents.

3.1 Local applicability of wind-driven currents

We use the two-parameter empirical model Eq. 1 to estimate Ekman Currents (u_e, v_e) (Niiler and Paduan, 1995; Sudre and Morrow, 2008),

$$(u_e + iv_e) = Be^{i\theta}(\tau_x + i\tau_y) \tag{1}$$

where τ_x and τ_y denote zonal and meridional wind stress, respectively. In the latitudinal bands of $25°S - 90°S$ and $25°N - 90°N$, we follow the amplitude $B = 0.3 ms^{-1}pa^{-1}$ and the vectoring angle θ of $55°$ relative to the wind stress direction. In the vicinity of the equator $25°S - 25°N$, the latitude-dependent parameters B and θ derived by Lagerloef et al. (1999) are adopted. These parameters are related to the Coriolis force parameter f, the water density $\rho = 1025 kgm^{-3}$, the linear drag coefficient $r_e = 2.15 \times 10^{-4} ms^{-1}$, and the friction depth $h_e = 32.5m$,

$$B = \frac{1}{\rho}(r_e^2 + f^2h_e^2)^{\frac{1}{2}}, \qquad \theta = arctan(\frac{fh_e}{r_e}) \tag{2}$$
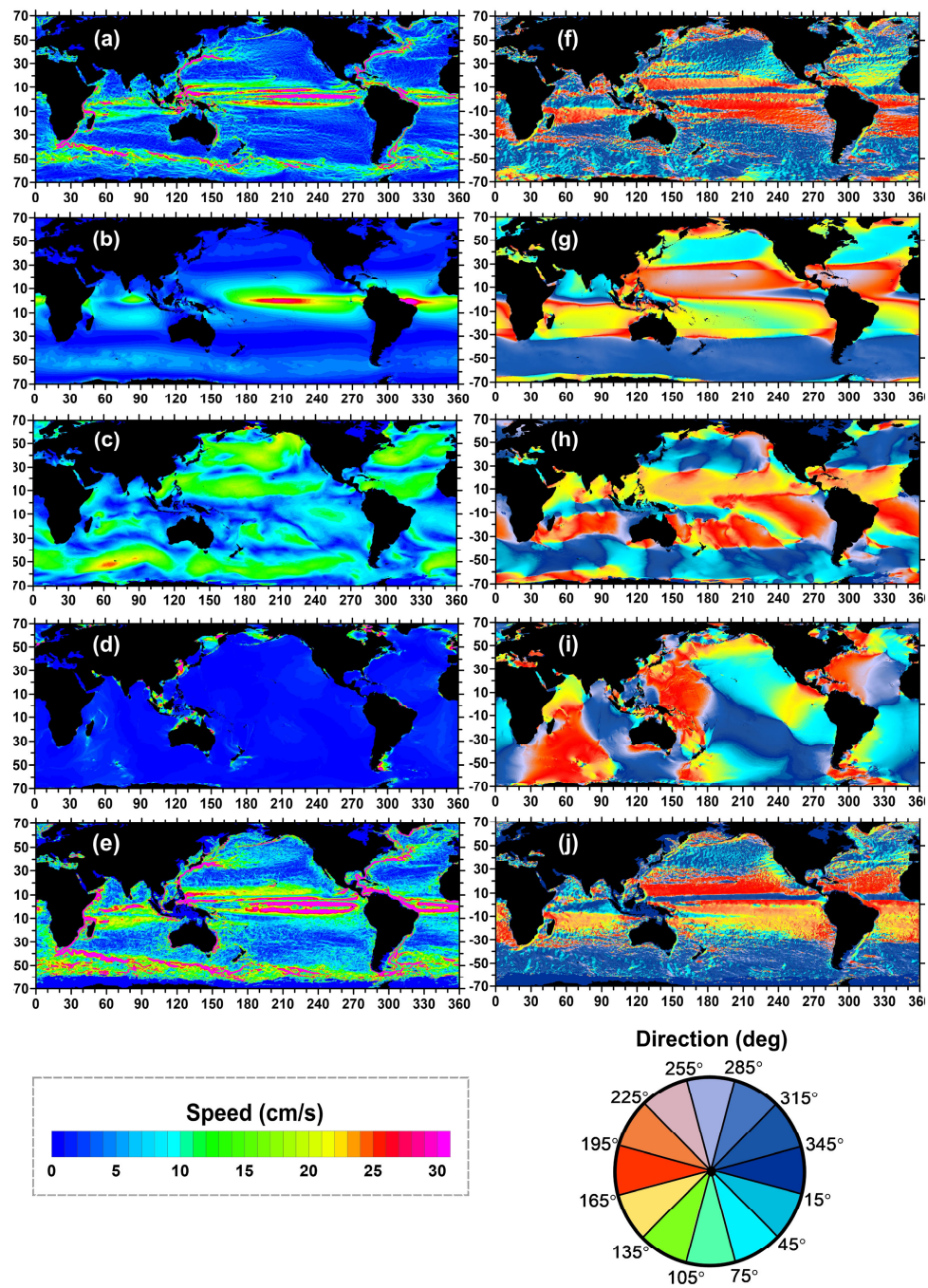
Figure 2. Global annual climatological flow fields. The left column represents flow speed of (a) geostrophic currents for 1999-2019, (b) Ekman currents for 1999-2019, (c) Stokes drift for 2013-2019, (d) tidal currents for 2013-2019, and (e) drifter observations for 1999-2019. While the right column is the flow direction.

Fig. 2 illustrates a climatological annual mean of Ekman currents alongside the geostrophic, Stokes, and tidal components. It is noteworthy that the uncertain assessment scheme of parameters B and θ within the equatorial band, as proposed by Lagerloef et al. (1999), seems to lead to elevated Ekman current velocities, contradicting the theory of a calm belt near the equator. In previous studies, geostrophic wind-driven velocities, derived by subtracting the geostrophic component from the drifting buoy velocities, have been utilized to calibrate parameters B and θ through least squares fitting. The friction depth of wind-driven currents (or Ekman depth) exhibits local adaptability, ranging from a few meters to a hundred meters, depending on wind stress intensity and the viscosity coefficient of seawater. Verification is essential to ensure that the mixing depth of the Ekman layer reaches the vertical position of the drogue (15 m). According to Van Meurs and Niiler (1997) and Lagerloef et al. (1999) proposed the linear steady momentum balance

$$\tau_y = \rho(fh_e u + r_e v), \qquad \tau_x = \rho(r_e u - fh_e v), \tag{3}$$

the friction depth h_e of Ekman currents can be calculated by

$$h_e = \frac{1}{f}\frac{\tau_y u - \tau_x v}{\rho(u^2 + v^2)}, \tag{4}$$

where u and v represent geostrophic vectors obtained by removing geostrophic velocities from drifters' observations of the monthly climate state. As shown in Fig.,3, with the deepening of Ekman's depth h_e, the correlation between ocean current velocities at different scales and drifter velocities exhibits a trend of initially increasing and then decreasing. This trend may be attributed to the sharp decline in the number of drifter observations after the validation of wind-driven friction depth. Considering the location of drogue drifters, the correlation between ocean components and drifter observations, along the variability in drifter observations, a friction depth of 15m was employed as the minimum threshold for filtering Ekman currents.
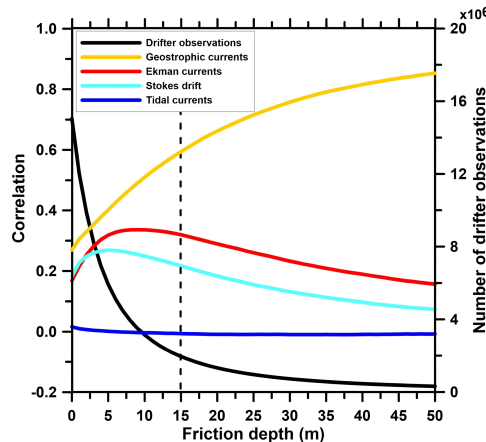
Figure 3. The correlation between four flow fields and observed velocity of drifters (left axis), and the number of drifter observations (the black line) varying with Ekman depth h_e (right axis).

3.2 Decay scales of Stokes drift and tidal currents

The reanalysis of Stokes drift and tidal currents u0 cover $0m$ vertically and require attenuation through the empirical percentage method, as follows:

$$u = u_0(1 - c\%), \tag{5}$$

This function is related to a decay scale c. Additionally, there is a theoretical decay equation for Stokes drift that can be expressed as

$$u_s = u_{s0} exp(2kz), \tag{6}$$

where u_{s0} denotes the surface Stokes drift, z is the profile derived from a monochromatic wave with wavenumber k and wavelength $\lambda = 2\pi/k$ (Kukulka and Harcourt, 2017). As depicted in Fig. 4, the correlation between drifter observations and various vector combinations of geostrophic, Ekman, tidal currents, and Stokes drift demonstrates a continuous increase in depth when utilizing the theoretical formula. Conversely, for tides, the correlation coefficient reaches its peak at an 80% attenuation when employing the percentage decay method. Consequently, the 80% decay ratio is applied to attenuate Stokes drift and tidal currents before the subsequent estimation of surface currents.
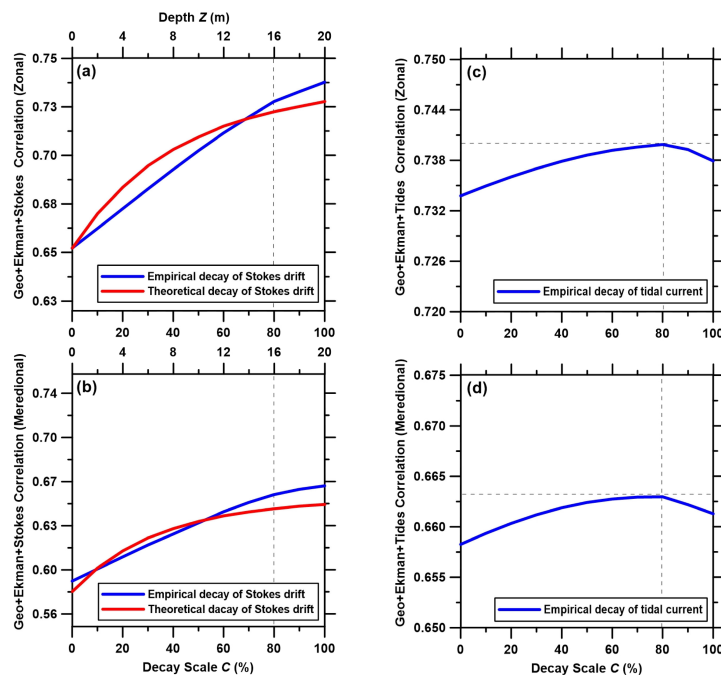
Figure 4. The zonal (top row) and meridional (bottom row) correlation of vector combinations of (a)-(b) geostrophic, Ekman currents, and Stokes drift, and (c)-(d) geostrophic, Ekman, and tidal currents.

3.3 Correlation analysis of ocean current components with drifter observations

A new drifter dataset is created by aligning pre-processed geostrophic currents, Ekman currents, Stokes drift, and tidal currents.
170 Subsequently, we calculate the Pearson correlation coefficient between ocean components and drifter observations. The Pearson correlation is formulated as follows:

$$Pearson = \frac{\sum_{i=1}^{n}(x_i - \overline{x})(y_i - \overline{y})}{\sqrt{\sum_{i=1}^{n}(x_i - \overline{x})^2}\sqrt{\sum_{i=1}^{n}(y_i - \overline{y})^2}} \tag{7}$$

where $\overline{x}$ and $\overline{y}$ are the mean values of the components and drifter, respectively. The calculated results of the Pearson correlation between ocean components and drifters are presented in Fig 5. What stands out in this figure is that the contribution of each
175 component to the flow field is evident. The geostrophic current emerges as a major component of the ocean surface current field, with a Pearson correlation coefficient reaching nearly 0.98 in regions characterized by strong and persistent currents along the western boundary. Wind-induced Ekman current play a significant role, particularly in the westerly zone of the northern and southern hemispheres, where the correlation of the geostrophic current is lower. This complementary feature underscores the importance of considering the coupling of multiple flows when reconstructing the current. Furthermore, the
180 wind-induced Ekman currents are less noticeable near the equator, which may be related to the calm zone in the tropics. Stokes drift demonstrates a substantial contribution, reaching up to 60% in the West Pacific. Tides primarily act in shallow coastal areas, with a maximum value of 0.5, consistent with their higher velocities along the coast.
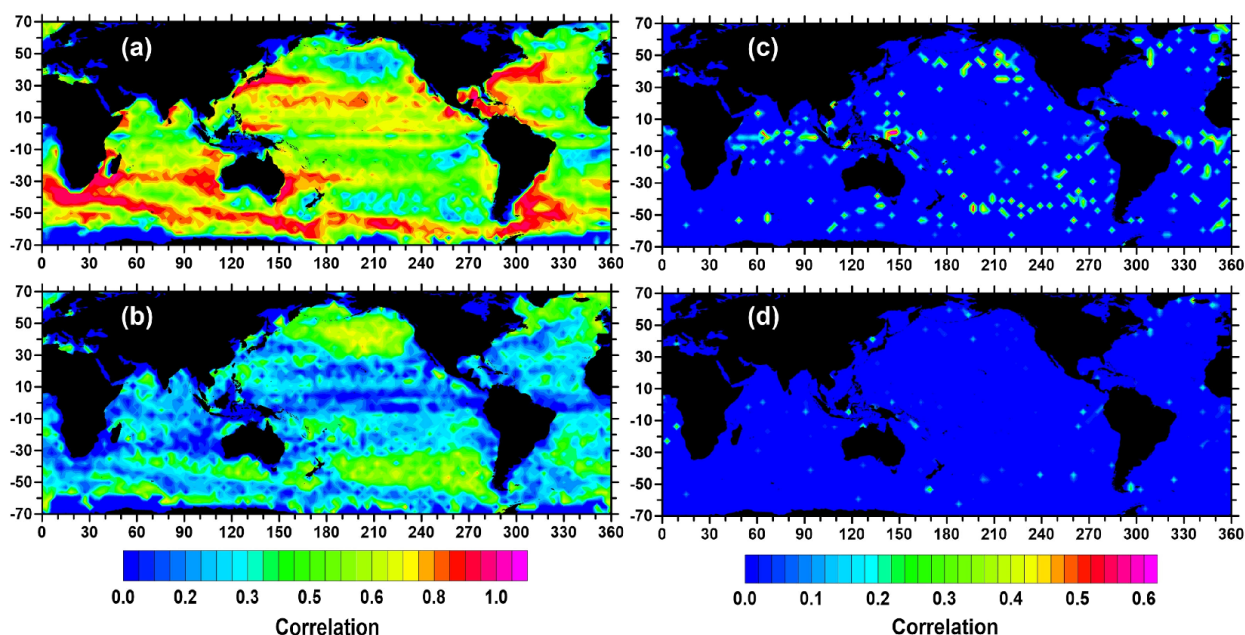
Figure 5. Geographical distribution of the Pearson correlation coefficient of (a) geostrophic current, (b) Ekman current, (c) Stokes drift, and (d) tidal current.

Reconstruction Model	Region			
	Southwest Maldives	Southwest Australia	Eastern Malaysia	Gulf of Mexico
Sub-GE	22.0333	**9.1091**	12.3418	7.9553
Sub-GES	20.9319	9.2731	**11.9773**	8.0693
Sub-GET	23.3724	9.2368	12.4657	**7.6361**
Sub-GEST	**20.6216**	9.3872	12.0061	7.8609

Table 1. The validation results of reconstructed current fields derived from the Sub-GE, Sub-GES, Sub-GET, and Sub-GEST models.

3.4 Polynomial coupling for estimating ocean surface current

To validate our approach for estimating ocean surface currents using the geostrophic current, Ekman current, Stokes drift, and tidal current, we constructed a polynomial function to model the functional relationship between these four components and the actual current. Given the seasonal and local variability in velocity and direction of the surface current, we first build polynomial regression on a 3° grid by season. Different flow field combinations (Sub-GE (Geostrophic-Ekman), Sub-GES (Geostrophic-Ekman-Stokes), Sub-GET (Geostrophic-Ekman-Tide), and Sub-GEST (Geostrophic-Ekman-Stokes-Tide)) are used to compare the performance of the four combined models. The data we utilized from 2006 to 2012, and verified the error of the models with root mean square error (RMSE), which mathematic as follows:

$$RMSE = \sqrt{\frac{1}{n}\sum_{i=1}^{n}(\widehat{y_i} - y_i)^2} \qquad (8)$$

Table 1 presents a regional comparison of the reconstruction errors for the sub-models. Different combinations of components contribute differently to regional reconstruction. For instance, in the Southwest Maldives, the GEST combination outperforms others, whereas in Eastern Malaysia, GEST proves to be more effective. This emphasizes the significance of considering coupled effects in various regions for oceanic current reconstruction.

Additionally, we compiled the global distribution of the zonal optimal sub-model and linear vector model selections during spring, as illustrated in Fig. 6. The statistics reveal that vector synthesis models account for approximately 38.1%, while regression models contribute to more than 60% globally. Meanwhile, Sub-GEST, Sub-GES, Sub-GET, and Sub-GE make up 11.1%, 16.2%, 13.8%, and 20.8%, respectively. Based on the regional estimates and the global distribution, reconstructing the global ocean surface current using the four components is a nonlinear task that necessitates consideration of region, different combinations, and seasons. Therefore, constructing a neural network emerges as an accurate and efficient method for ocean surface current reconstruction.

4 Multi-scale dynamics-informed neural network

Machine learning, a cornerstone of artificial intelligence, allows machines to discern rules gleaned from data. The decision tree, serving as a proficient nonlinear model, has the capability to assemble a forest through ensemble learning techniques.
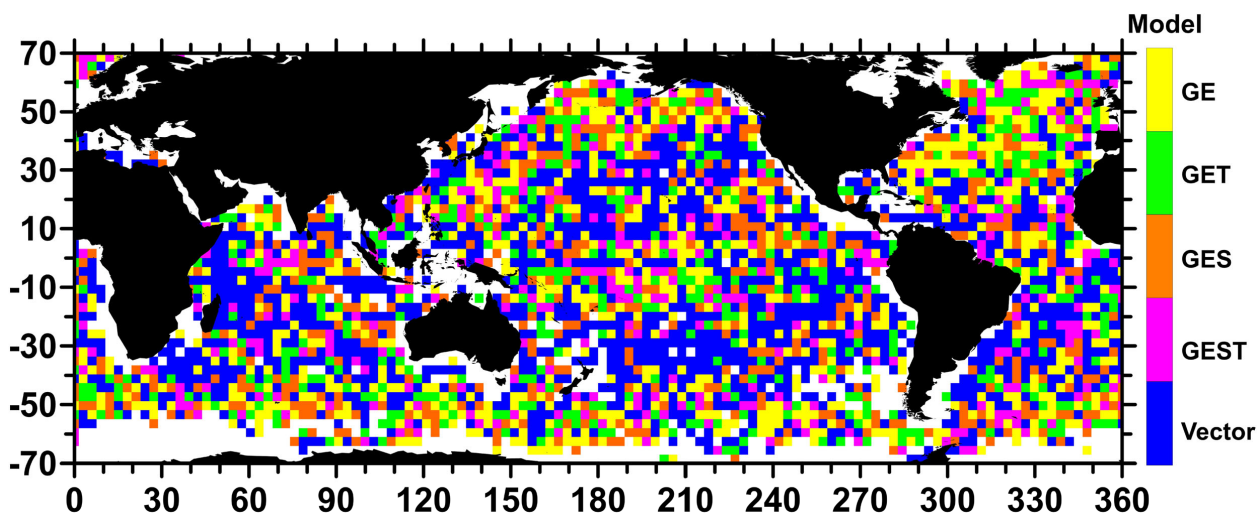
Figure 6. The global distribution of the zonal optimal sub-models combinations in spring.

The neural network, famous for its unmatched capacity for nonlinear fitting, empowers the machine to uncover latent features embedded within vast datasets. Drawing upon insights gleaned from the preceding analysis of the correlation and impact of multi-scale dynamics on modern reconstruction endeavors, we amalgamated the random forest and neural network to craft a model informed by multi-scale dynamics, christened GESTNet. The architecture of GESTNet is depicted in Fig. 7.
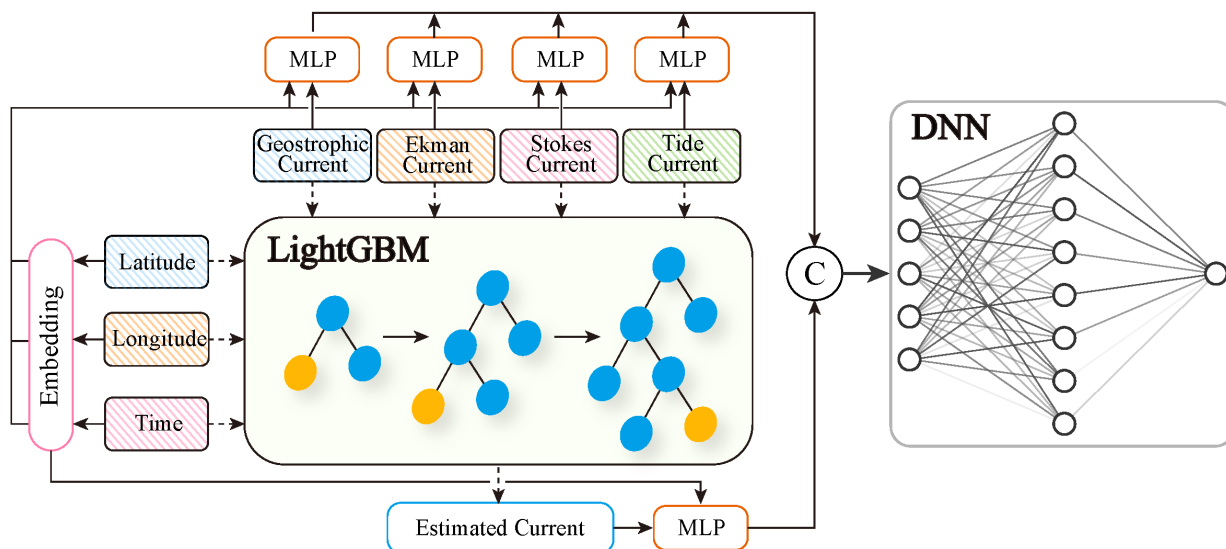
Figure 7. The architecture of the GESTNet. The dotted lines are the process of the LightGBM, and the full lines denote the pipeline of the neural network.

4.1 GESTNet

210 In light of the interaction of multiscale current dynamics, our objective is to construct the oceanic surface current utilizing these multiscale current components, which encompass time t, coordinate information i, j, geostrophic currents $G_{(u,v)}$, Ekman currents $E_{(u,v)}$, Stokes currents $S_{(u,v)}$, and tide currents $T_{(u,v)}$. Therefore, a function needs to be built for

$$c_{u,v} = \mathcal{F}(x_{u,v}), \quad x = \{t, i, j, G_{u,v}, E_{u,v}, S_{u,v}, T_{u,v}\} \tag{9}$$

where $c_{u,v}$ represents the reconstruction values. However, the geostrophic current, Ekman current, Stokes drift, and tidal current

215 exhibit varying resolutions and densities. Regardless of whether employing a tree-based or neural network approach, these data characteristics pose challenges to achieving accurate and effective reconstruction. Therefore, to ensure the highest data resolution, we organized all data into a 0.25 degree grid. Subsequently, these collated data are fed into the LightGBM model. LightGBM, a renowned model developed on the gradient boosting decision tree (GBDT), is employed. GBDT, an ensemble model, constructs a robust regression model by generating multiple weak regression trees. The depth and number of leaves in

220 the tree significantly impact model accuracy and generalization ability. Thus, during the iterative training of LightGBM, the incorporation of a penalty function becomes necessary to regulate leaf splitting. This formulation is expressed as

$$\Omega(f_t) = \gamma T + \frac{1}{2}\lambda \sum_{j=1}^{T} w_j^2 \tag{10}$$

where f_t represents the t-th tree, T denotes the number of leaf nodes, γ signifies the complexity cost introduced by new leaf nodes, and w_j^2 denotes the L2 regularization term of the leaf fraction. Given that LightGBM is an ensemble model, the f_t

225 governs the regression results. The output can be mathematically formalized as

$$\hat{y}_i^t = \sum_{k=1}^{t} f_k(x_i) = \hat{y}_i^{t-1} + f_t(x_i) \tag{11}$$

where $\hat{y}_i^t$ represents the regression value of the t-th tree. To attain the optimal LightGBM model, it is necessary to minimize Eq.(10) and Eq.(11), thereby minimizing the function

$$\mathcal{L} = \sum_{i=1}^{n} |y_i - \hat{y}_i^t| + \Omega(f_t) + C \tag{12}$$

230 Subsequently, leveraging the optimal LightGBM model, we can acquire the estimated current. Owing to the distinctive traits of the tree model, the regression value is constrained within the bounds of the training data's minimum and maximum values. However, the neural network possesses significant inference power, enabling it to address the aforementioned challenge. Consequently, we integrated the estimated current with the original data and formulated a neural network to identify the discrepancies between the estimated current and the real-world environment.

235 Within the neural network structure, we incorporated the estimated current, thereby transforming the ocean surface current reconstruction task into

$$\hat{c}_{u,v} = \hat{\mathcal{F}}(x_{u,v}), \quad x = \{t, i, j, G_{u,v}, E_{u,v}, S_{u,v}, T_{u,v}\} \tag{13}$$

Diverging from the LightGBM approach, these features cannot be directly inputted into the neural network. The current components require normalization, and the time and coordinate features need to be transformed into continuous space. Thus, we

240 employ the embedding method to embed the time, latitude, and longitude into continuous features, mitigating the issue of small feature disparities arising from normalization. Subsequently, we integrate the embedded time, latitude, longitude, and each current component into standard multilayer perceptrons (MLPs). These MLPs nonlinearly map each current component according to the time and coordinate, extracting hidden features. Moreover, MLPs possess the capability to expand the input resolution to a certain extent, enhancing reconstruction accuracy. Following this, we construct a deep neural network (DNN) to

245 model the relationship between components and the physical environment, learning the disparity between real and estimated currents. Considering the influence of multi-scale dynamics on surface currents, we account for the differing effects of current components at different locations when constructing the DNN and employing the MLP for data mapping. Furthermore, the concatenation of all embedded data into the DNN enables the neural network to not only consider the meridional current but also refer to the indirect interaction of zonal current while reconstructing the meridional value.

250 ### 4.2 Training Detail

The LightGBM is configured with 1024 leaves, 100 estimators, and 500 iterations. To prevent overfitting, we employ an early stopping round of 5. As for the neural network, we conduct 50 training epochs, initialize the learning rate to 0.0001, and set the batch size to 4096. To expedite model convergence, we adopt the cosine annealing learning rate adjustment strategy with an adjustment step of 500. For parameter optimization in the neural network, we utilize the AdamW optimizer and employ L1

255 loss for loss calculation. This loss function helps mitigate the impact of outliers and is formulated as

$$L1_{L}oss = \sum_{i=1}^{n} |y_i - \hat{y}_i| \tag{14}$$

Considering the significant variations in current velocity and direction across different seasons in the equatorial region, we conducted separate training sessions for the LightGBM and neural network for each quarter to ensure accurate reconstruction.

4.3 Compare Method and Production

260 To ascertain the reconstruction accuracy of our proposed model, we compare the results with various methods and products, including:

Optimal GEST. Construct polynomial regression and vector combination models for various combinations of multi-scale flow fields within each $3°$ grid. Through model error validation, identify the optimal combination GEST reconstruction model with the lowest reconstruction error and the highest contribution in each subregion. Utilize the optimal GEST reconstruction model

265   for the inversion of flow field data at spatial resolutions of $1°$ and $0.25°$.

OSCARCurrent. The Ocean Surface Current Analysis Real-time (OSCAR) project, funded by the National Aeronautics and Space Administration (NASA) of the United States, predominantly utilizes satellite remote sensing data to derive information on sea surface wind fields, sea surface height gradients, and sea surface temperature distributions. These datasets are then utilized in the inversion of geostrophic, wind-driven, and thermally-induced wind dynamics for ocean surface current recon-

270   struction. The ocean surface velocity files are formatted in Network Common Data Form (NetCDF), comprising total zonal u and meridional v velocities, as well as zonal ug and meridional geostrophic vg components.

GlobCurrent. The GlobCurrent project stands as a cornerstone initiative within the European Space Agency's Earth Observation Programme's fourth phase, committed to the progressive refinement of quantitative estimation of ocean surface currents through the synergistic integration of satellite sensors. The dataset comprises surface geostrophic currents, Ekman currents

275   at both surface and 15 meters depth, along with composite flows arising from the amalgamation of geostrophic and Ekman currents. All components maintain a spatial resolution of 25 kilometers, with geostrophic currents observed at a temporal resolution of 1 day, and Ekman currents and composite flows resolved at 3-hour intervals.

5   Results

The ocean surface current exhibits significant variability across different regions. Taking into account both the direction and

280   velocity of the current, the root mean square error (RMSE) and the mean absolute error were employed to assess the accuracy of the reconstruction results and the performance of our proposed model. Due to the distinct seasonal characteristics of equatorial currents, we trained the GESTNet on quarterly data encompassing both zonal and meridional currents. Consequently, we trained eight models to reconstruct data for a full year. For a more robust comparison of reconstruction accuracy, we utilized data from 2013 to 2017 for verification. First of all, the reconstruction performance is assessed from a global perspective.

285   Fig. 8 illustrates the RMSE of the synthesized meridional and zonal values for the entire validation dataset obtained from Global Current, OSCARCurrent, Optimal GEST, and GESTNet, within a $3° \times 3°$ grid.

As illustrated in Fig. 8, it becomes evident that the utilization of a combination of geographical currents, Ekman currents, Stokes currents, and tidal currents is imperative and highly effective for the comprehensive reconstruction of global ocean surface currents. The reconstruction approach, anchored in the concept of multiscale currents, possesses the capability to enhance

290   the precision of both nearshore and equatorial currents. Furthermore, the integration of machine learning methods can harness the full potential of multiscale currents in reconstructing ocean surface currents. To convincingly verify the significance of multiscale currents and the reconstruction performance of GESTNet, we computed the MAE and the RMSE between the comparative method and the actual production in the u, v, and $\sqrt{u^2 + v^2}$ values. Comparing the numerical values in Table 2, we can discern that employing polynomial regression to reconstruct surface oceanic currents based on multiscale current composi-

295   tion yields accuracy levels close to those of GlobCurrent. The Optimal GEST model exhibits a 5% reduction in error compared to OSCARCurrent. These observations underscore the significance of utilizing multiscale currents in the reconstruction process. Nevertheless, upon utilizing the machine learning approach for current reconstruction, the specifically designed model,
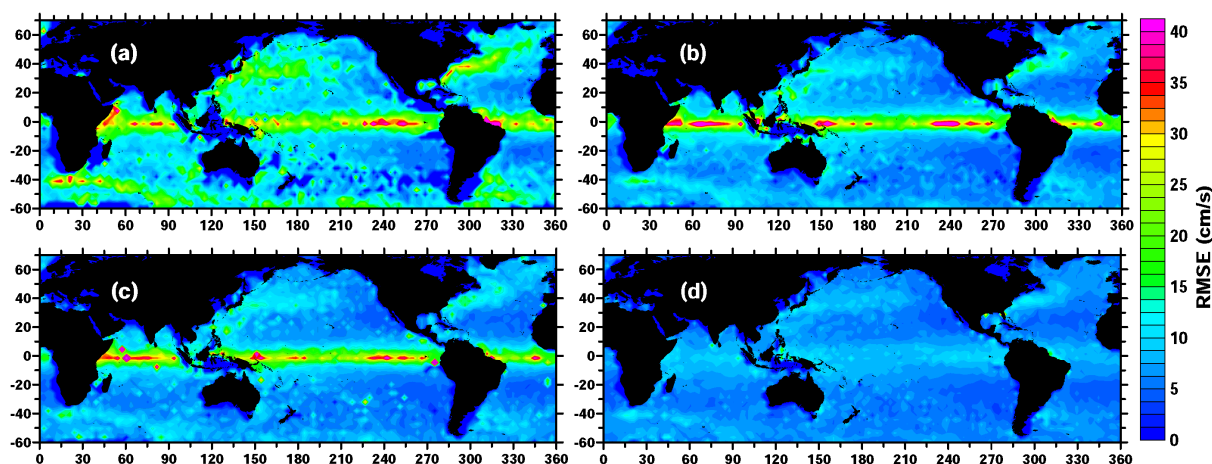
Figure 8. The distribution of the global RMSE $\sqrt{u^2 + v^2}$ for GlobCurrent, OSCARCurrent, Optimal GEST, and GESTNet, calculated using data from the Drifters. (a) The RMSE of OSCARCurrent. (b) The RMSE of GlobCurrent. (c) The RMSE of Optimal GEST. (d) the RMSE of GESTNet.

Oceanic Currents	u		v		$\sqrt{u^2 + v^2}$	
	MAE	RMSE	MAE	RMSE	MAE	RMSE
Production						
GlobCurrent	14.407	19.377	13.579	18.334	14.314	19.411
OSCARCurrent	15.717	21.036	14.377	19.310	16.94	22.527
Model						
Optimal GEST	14.908	19.926	13.803	18.564	14.808	19.995
GESTNet	**5.040**	**6.808**	**5.612**	**7.466**	**5.222**	**7.029**

Table 2. The MAE and RMSE of u, v, $\sqrt{u^2 + v^2}$ across GlobCurren, OSCARCurrent, OPtimalGEST, and GESTNet. The minimum error is highlighted in bold font.

GESTNet, exhibits exceptional performance. For instance, when comparing the $\sqrt{u^2 + v^2}$ values of GlobCurrent, OSCAR-Current, and Optimal GEST, the RMAE decreases by approximately 63%, 68%, and 64%, respectively. The MAE experiences
300 improvements of around 65%, 58%, and 63%, respectively. Thus, the utilization of machine learning or deep learning methods empowers the task of oceanic current reconstruction, leading to enhanced accuracy in the reconstruction process.

Ocean currents exhibit seasonal variations, including differences in velocity and flow direction at the equator between summer and winter. Moreover, it is crucial to assess whether the reconstruction results of GESTNet exhibit seasonal deviations. Therefore, we collected the RMSE and MAE for the four quarters across four models, as presented in Table 3, and drew the
305 global distribute RMSE of GESTNet shown in Fig. 9. The figures clearly demonstrate that regardless of the zonal or merid-
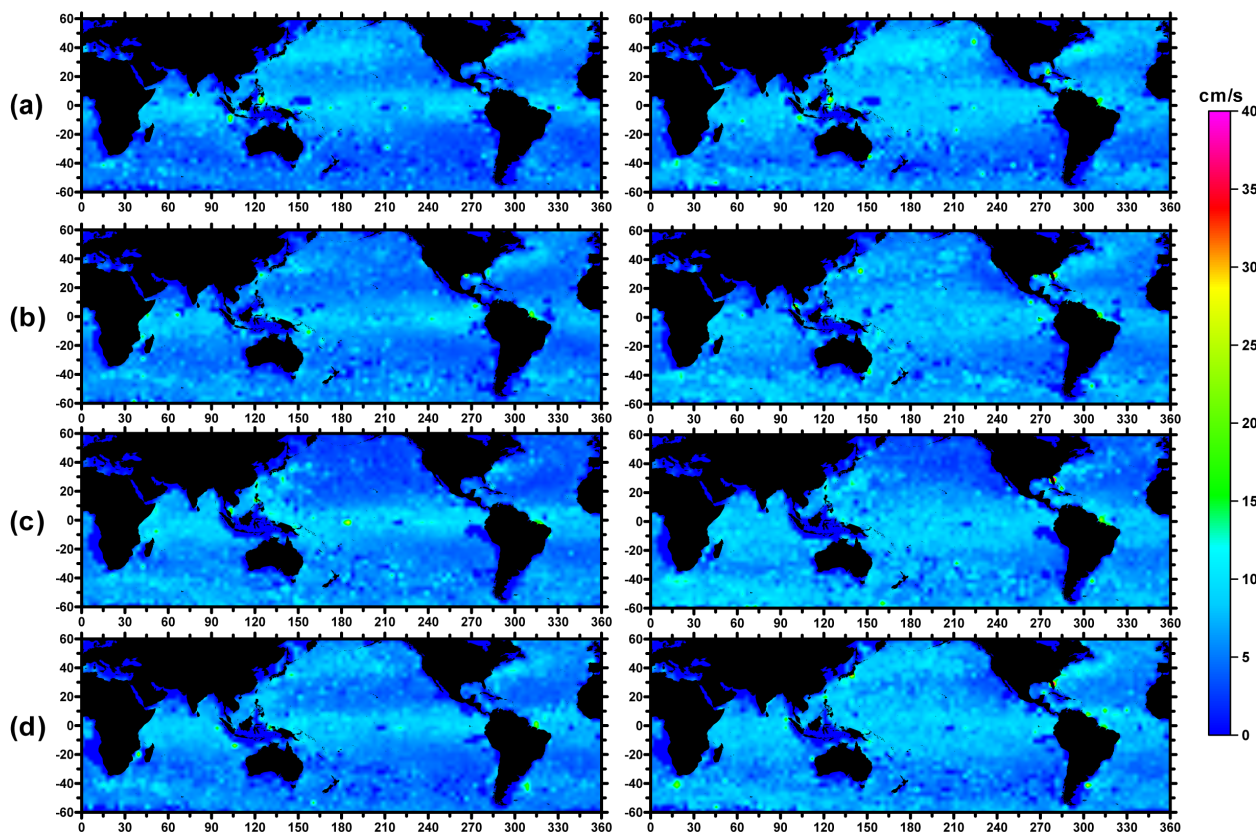
Figure 9. RMSE of the reconstructed ocean surface current using GESTNet. The left panels depict the zonal component, while the right panels present the meridional current. Lines (a), (b), (c), and (d) correspond to the RMSE values for quarters Q1, Q2, Q3, and Q4, respectively.

ional components, the RMSE of the reconstructed current consistently stays below 15 cm/s, typically around 5 cm/s. Moreover, GESTNet consistently displays significant performance across all quarters. Meanwhile, as shown in Table 3, the MAE hovers around 5 cm/s, while the RMSE fluctuates around 7 cm/s. These findings illustrate that the reconstructed currents by GEST-Net do not exist in seasonal deviations. When compared to other oceanic currents and models, GESTNet exhibits exceptional reconfiguration performance. Across different seasons and components, both the MAE and RMSE consistently remain lower than those of the GlobCurrent, OSCARCurrent, and Optimal GEST. For instance, in the case of the u component, the relative improvement of MAE across the four quarters is 64%, 67%, 64%, and 64%, respectively. In order to assess the global relative improvement in the reconstruction of oceanic currents by GESTNet, we computed the degree of global relative improvement between GESTNet and both GlobCurrent and OptimalGEST as shown in Fig. 10.

In Fig.,10, the most significant improvement is observed with GESTNet in equatorial regions. Based on statistics, the relative improvement degree of zonal current and meridional current at the equator is 41.145% and 41.839%, respectively. This demonstrates the capacity of artificial intelligence methods to ameliorate the geostrophic imbalance of the current in the equatorial

Oceanic Currents	Component	Q1		Q2		Q3		Q4	
		MAE	RMSE	MAE	RMSE	MAE	RMSE	MAE	RMSE
Production									
GlobCurrent	u	14.702	19.687	14.434	19.387	14.327	19.278	14.407	19.377
	v	13.788	18.532	13.593	18.318	13.508	18.227	13.579	18.334
	$\sqrt{u^2+v^2}$	14.637	19.778	14.360	19.450	14.230	19.296	14.314	19.411
OSCARCurrent	u	15.926	21.155	15.668	21.036	15.588	20.874	15.717	21.036
	v	14.570	19.482	14.367	19.31	14.289	19.193	14.377	19.310
	$\sqrt{u^2+v^2}$	17.252	22.776	16.917	22.527	16.787	22.330	16.940	22.527
Model									
OPtimalGEST	u	15.092	20.024	14.863	19.799	14.785	19.776	14.908	19.926
	v	13.920	18.57	13.736	18.347	13.697	18.444	13.803	18.564
	$\sqrt{u^2+v^2}$	15.134	20.258	14.814	19.879	14.669	19.841	14.808	19.995
GESTNet	u	**5.168**	**6.987**	**4.761**	**6.411**	**5.157**	**6.956**	**5.048**	**6.829**
	v	5.759	7.652	5.314	7.050	5.704	7.593	5.644	7.519
	$\sqrt{u^2+v^2}$	5.343	7.194	4.914	6.590	5.338	7.168	5.269	7.115

Table 3. The MAE and RMSE of zonal and meridional currents for various productions and models across different seasons. The optimal u is highlighted in bold, the optimal v is underscored, and the $\sqrt{u^2+v^2}$ is depicted with a wavy line.

region. Furthermore, from Fig. 10, it is evident that GESTNet not only enhanced the accuracy of flow field reconstruction in the equatorial region but also improved accuracy in regions with strong flows, such as the Kuroshio region and the eastern coast of North America. Subsequently, we computed the relative improvement degree in non-equatorial regions, which amounted to 17.775% in the u component and 24.524% in the v component.

From Fig. 8 and Fig. 10, the errors vary across different latitudes. Therefore, in addition to assessing the model's performance and reconstructing the accuracy from a global distribution perspective, we calculated the zonal RMSE states illustrated in Fig. 11. Observation from Fig. 11 reveals that reconstruction incorporating geographical, Ekman, Stokes, and tidal currents enhances current reconstruction accuracy across most regions, affirming the feasibility, validity, and reliability of ocean surface current reconstruction using these components. Compared to GlobCurrent, GESTNet improves accuracy by 35.175% between $20°N$ and $20°S$. Moreover, direct observation from the figure indicates that GESTNet reduces errors in ocean surface current reconstruction between $60°N$ and $60°S$. Between $60°S$ and $20°S$, GESTNet exhibits a 40.038%, 21.340%, and 20.793% improvement over OSCARCurrent, GlobCurrent, and Optimal GEST, respectively. Similarly, between $20°N$ and $60°N$, GESTNet achieves a comparable reduction in errors compared to the Southern Hemisphere, surpassing OSCARCurrent, GlobCurrent, and Optimal GEST by 41.431%, 18.185%, and 17.948%, respectively. Notably, at the equator, GESTNet, employing machine learning techniques, achieves a 37.356%, 42.257%, and 33.947% improvement in reconstruction accuracy
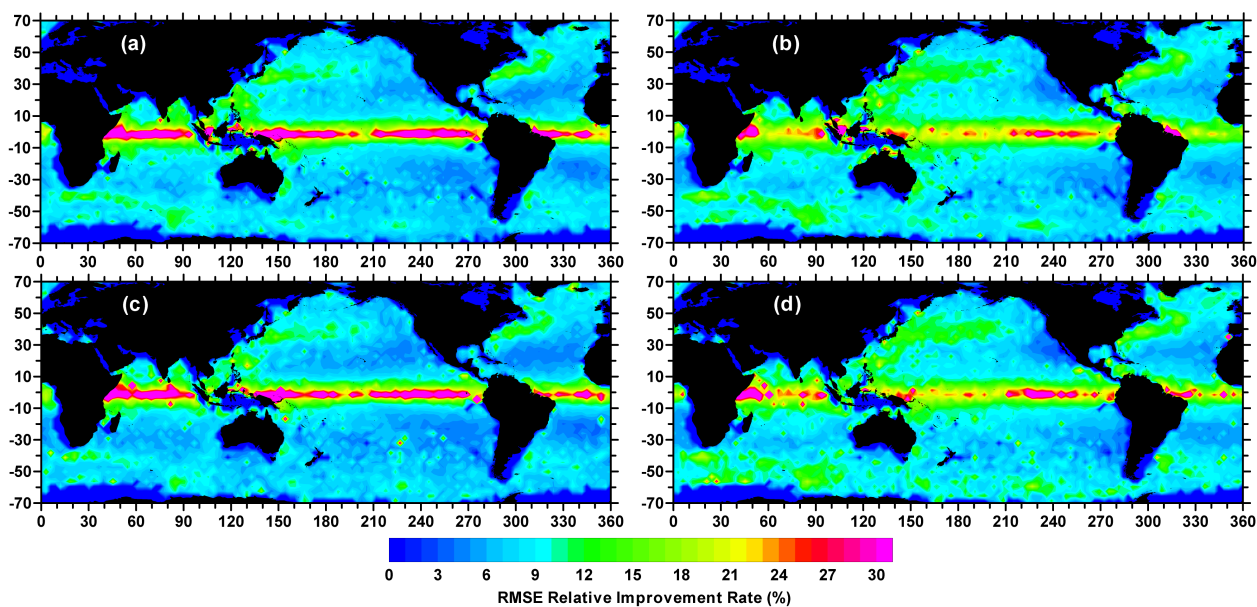
Figure 10. The global relative improvement degree between GESTNet and both GlobCurrent and OptimalGEST is analyzed. (a) GESTNet improvement degree of zonal current compared with GlobCurrent, (b) GESTNet improvement degree of meridional current compared with GlobCurrent, (c) GESTNet improvement degree of zonal current compared with Optimal GEST, and (d) GESTNet improvement degree of meridional current compared with Optimal GEST.
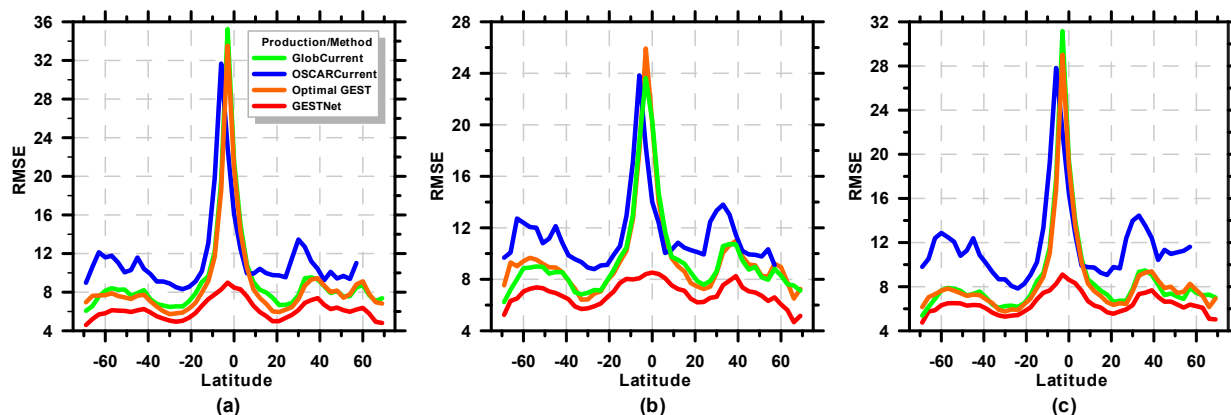
Figure 11. The zonal RMSE distribution of GlobCurrent, OSCARCurrent, Optimal GEST, and GESTNet. (a) The RMSE of u. (b) The RMSE of v. (c) The RMSE of $\sqrt{u^2 + v^2}$.
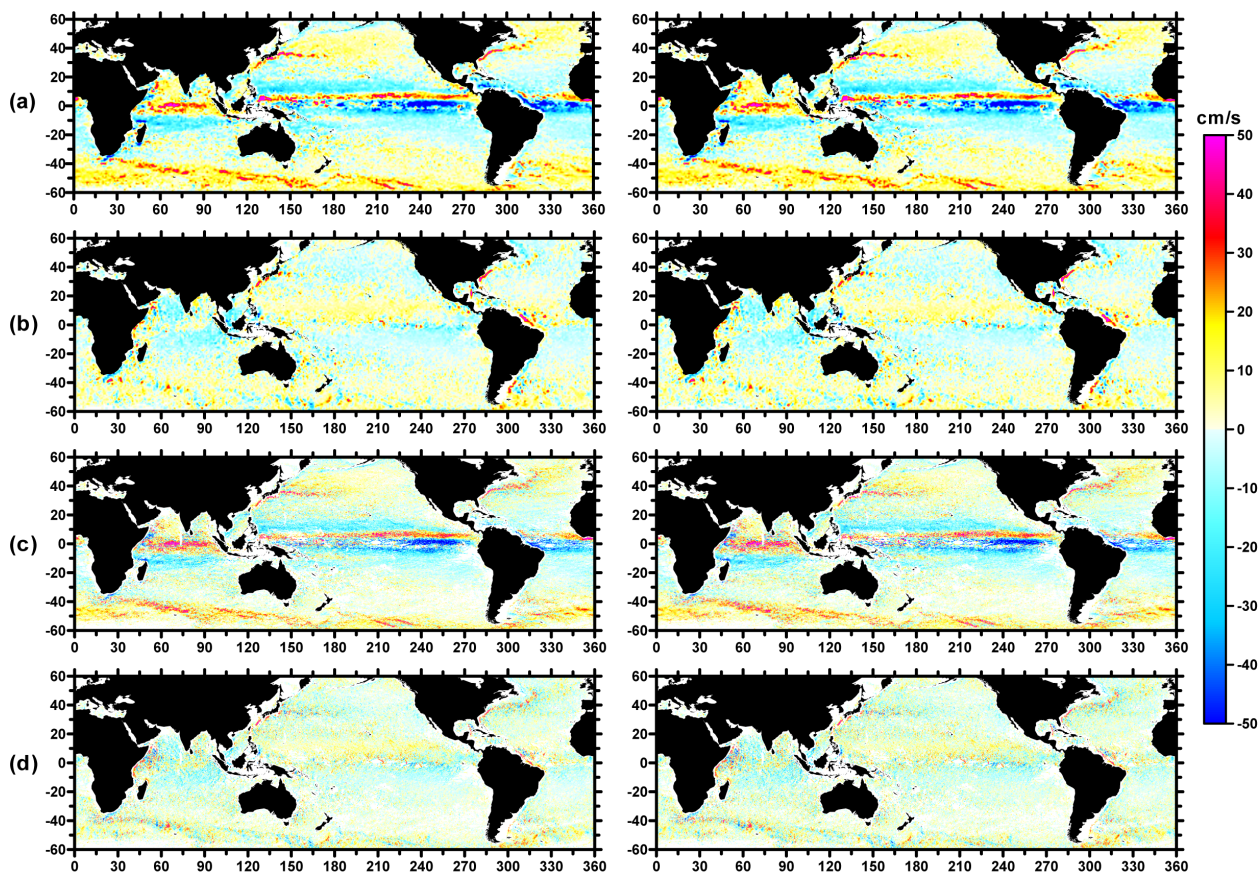
Figure 12. The reconstructed global ocean surface current by GESTNet and the truth observation current by Drifter in $0.25°$ and $1°$. (a) Reconstruction results (left) of the $1°$ resolution u component and actual observations (right). (b) same as (a) but for v component. (c) Left is $0.25°$ u component reconstruction results, while the right is observed by Drifter. (d) same as (c) but for v component.

compared to GlobCurrent, OSCARCurrent, and Optimal GEST, respectively. These findings confirm the effectiveness and superior reconstruction performance of machine learning methods in reconstructing sea surface flow fields.

335   Finally, we examine the resemblances and disparities between the reconstructed current and the Drifter flow field, as shown in Fig. 12. Fig. 12 displays the 2013-2017 mean reconstruction results of $0.25°$ and $1°$, and actual Drifter observations. Both the u and v components of the current reconstructed by GESTNet exhibit substantial consistency with those observed by drifters in terms of velocity and direction. Consequently, based on Fig. 12 and the preceding analysis of the reconstruction outcomes, it can be asserted that the reconstruction results achieved by GESTNet demonstrate high accuracy and reliability.

6   Conclusions

Ocean surface currents exhibit multi-scale dynamic processes, prominently featuring large-scale geostrophic circulation and wind-induced Ekman flow, while often disregarding small-scale wave phenomena. With this understanding, we devised a novel multiscale-dynamics-informed model grounded in machine learning and deep learning techniques to produce a new product of the global ocean current at a depth of 15 meters, integrating Geostrophic, Ekman, Stokes, and Tidal multiscale currents. This research endeavor culminates in the following conclusions:

- The multi-scale dynamics-based GESTNet product of ocean surface currents demonstrates reliability, evidenced by the reduced RMSE of the $0.25°$ resolution product, which is approximately 15.498 cm/s lower than that of the OSCAR product and 12.382 cm/s lower than that of the GlobCurrent.

- Acknowledging the challenge posed by geostrophic failure at the equator, we incorporated the LightGBM model into GESTNet to provide an auxiliary estimate, thereby enhancing the accuracy of the current reconstruction and mitigating the local failure of the geostrophic effect in the equatorial region.

- The interaction among multi-scale currents guided the development of GESTNet, resulting in a substantial improvement in the accuracy of oceanic surface current reconstruction. Specifically, in the equatorial region, the improvement compared to GlobCurrent is nearly 37%.

It is important to highlight that the GEST current product is adept for conditions where Ekman currents influence up to a depth of 15 meters, contrasting with existing ocean current estimation products. Furthermore, the proposed GEST dataset demonstrates superior performance at low to mid-latitudes independently, without relying on assimilated drifter observations. However, it is noteworthy that GESTNet is designed to model different seasons' current reconstruction. Additionally, multi-scale currents are preprocessed before being inputted into the model. Therefore, in the future, it is imperative to incorporate complex mechanisms such as planetary waves, mesoscale eddies, and sub-mesoscale processes into standard ocean models and parameterize them to enhance the reconstruction accuracy of sea surface currents. Furthermore, constructing a multimodal model to reconstruct ocean surface currents end-to-end throughout the year is also a promising avenue for future research.

Code availability.   The Code is abaliable at GitHub: https://github.com/AI4Ocean/GESTNet

Data availability.

All data used in this study are publicly available and are listed in Table 4. The TPXO9-atlas for tidal currents is available for academic research and other non-commercial uses under previous registration from https://www.tpxo.net/global/tpxo9-atlas (Egbert and Erofeeva, 2002). The GEST product (Ge and Wang, 2024) produced in this research can be found at https://doi.org/10.5281/zenodo.11142408.

Dataset	Link	Citation
Geostrophic Current	https://data.marine.copernicus.eu/product/ SEALEVEL_GLO_PHY_L4_MY_008_047/	Pujol et al. (2016)
Ocean Waves Reanalysis Data	https://data.marine.copernicus.eu/product/ GLOBAL_MULTIYEAR_WAV_001_032/	Law-Chune et al. (2021)
WindSat Products	https://www.remss.com/missions/windsat/	Wentz et al. (2013)
Quikscat Products	https://www.remss.com/missions/qscat/	Ricciardulli et al. (2011)
Global Drifter Data	https://www.aoml.noaa.gov/phod/gdp/hourly_data. php	Elipot et al. (2022)
OSCAR Current	https://search.earthdata.nasa.gov/downloads/ 6873202440	Johnson et al. (2007)
GlobCurrent Product	https://tds0.ifremer.fr/thredds/GLOBCURRENT/ GLOBCURRENT.html?\dataset= GLOBCURRENT-L4-CUREUL_15M-ALT_ SUM-V03.0	Rio et al. (2014)

Table 4. Remotely sensed, in situ, and reanalysis data sets used in this paper.

Author contributions. Linyao Ge drafted the manuscript, developed the data processing, and designed the experiment. Guiyu Wang designed
370   the Optimal GEST model and produced the first version of the GEST production. Ge Chen contributed to conceptualizing the project, supervising, reviewing, and editing the paper. Chuanchuan Cao developed the data processing and edited the paper. Xiaoyan Chen edited and reviewed the paper. Baoxiang Huang supervised and reviewed the paper.

Competing interests. The authors declare that we have no known competing financial interests or personal relationships that could have appeared to influence the work reported in this paper.

375   *Acknowledgements.* This work was jointly supported by the National Natural Science Foundation of China (Grant No. 42030406, 42276203), the Laoshan Laboratory(No.LSKI202204302), and the Natural Science Foundation of Shandong Province (No.ZR2021MD001).

References

Bi, F., Wu, K., and Zhang, Y.: The effect of stokes drift on ekman transport in the open sea, Acta Oceanologica Sinica, 31, 12–18, https://doi.org/10.1007/s13131-012-0249-1, 2012.

380 Bi, K., Xie, L., Zhang, H., Chen, X., Gu, X., and Tian, Q.: Accurate medium-range global weather forecasting with 3D neural networks, Nature, 619, 533–538, https://doi.org/10.1038/s41586-023-06185-3, 2023.

Bonjean, F. and Lagerloef, G. S. E.: Diagnostic model and analysis of the surface currents in the tropical pacific ocean, Journal of Physical Oceanography, 32, 2938–2954, https://doi.org/10.1175/1520-0485(2002)032<2938:DMAAOT>2.0.CO;2, 2002.

Bowen, M. M., Emery, W. J., Wilkin, J. L., Tildesley, P. C., Barton, I. J., and Knewtson, R.: Extracting multiyear surface currents from

385 sequential thermal imagery using the maximum cross-correlation technique, Journal of Atmospheric and Oceanic Technology, 19, 1665–1676, https://doi.org/10.1175/1520-0426(2002)019<1665:EMSCFS>2.0.CO;2, 2002.

Caniaux, G., Belamari, S., Giordani, H., Paci, A., Prieur, L., and Reverdin, G.: A 1 year sea surface heat budget in the northeastern atlantic basin during the POMME experiment: 2. flux optimization, Journal of Geophysical Research: Oceans, 110, 2004JC002695, https://doi.org/10.1029/2004JC002695, 2005.

390 Chapman, C. and Charantonis, A. A.: Reconstruction of subsurface velocities from satellite observations using iterative self-organizing maps, IEEE Geoscience and Remote Sensing Letters, 14, 617–620, https://doi.org/10.1109/LGRS.2017.2665603, 2017.

Choi, J.-K., Yang, H., Han, H.-J., Ryu, J.-H., and Park, Y.-J.: Quantitative estimation of suspended sediment movements in coastal region using GOCI, Journal of Coastal Research, 165, 1367–1372, https://doi.org/10.2112/SI65-231.1, 2013.

Dohan, K. and Maximenko, N.: Monitoring ocean currents with satellite sensors, Oceanography, 23, 94–103,

395 https://doi.org/10.5670/oceanog.2010.08, 2010.

Egbert, G. D. and Erofeeva, S. Y.: Efficient inverse modeling of barotropic ocean tides, Journal of Atmospheric and Oceanic Technology, 19, 183–204, https://doi.org/10.1175/1520-0426(2002)019<0183:EIMOBO>2.0.CO;2, 2002.

Ekman, V. W.: On the influence of the earth's rotation on ocean-currents, Ark. Mat. Asto. Fys., 2, 1–53, 1905.

Elipot, S., Lumpkin, R., Perez, R. C., Lilly, J. M., Early, J. J., and Sykulski, A. M.: A global surface drifter data set at hourly resolution,

400 Journal of Geophysical Research: Oceans, 121, 2937–2966, https://doi.org/10.1002/2016JC011716, 2016.

Elipot, S., Sykulski, A., Lumpkin, R., Centurioni, L., and Pazos, M.: Hourly location, current ve-locity, and temperature collected from Global Drifter Program drifters world-wide. NOAA -National Centers for Environmental Information, https://doi.org/10.25921/x46c-3620, 2022.

Garçon, V. C., Oschlies, A., Doney, S. C., McGillicuddy, D., and Waniek, J.: The role of mesoscale variability on plankton dynamics in the north atlantic, Deep Sea Research Part II: Topical Studies in Oceanography, 48, 2199–2226, https://doi.org/10.1016/S0967-

405 0645(00)00183-1, 2001.

Ge, L. and Wang, G.: GEST Ocean Surface Current 2.0, https://doi.org/10.5281/zenodo.11142408, 2024.

Ge, L., Huang, B., Chen, X., and Chen, G.: Medium-range trajectory prediction network compliant to physical constraint for oceanic eddy, IEEE Transactions on Geoscience and Remote Sensing, 61, 1–14, https://doi.org/10.1109/TGRS.2023.3298020, 2023.

González-Haro, C. and Isern-Fontanet, J.: Global ocean current reconstruction from altimetric and microwave SST measurements, Journal

410 of Geophysical Research: Oceans, 119, 3378–3391, https://doi.org/10.1002/2013JC009728, 2014.

Guan, S., Deng, H., Wang, Y., and Yang, X.: NeuroFluid: Fluid Dynamics Grounding with Particle-Driven Neural Radiance Fields, in: Proceedings of the 39th International Conference on Machine Learning, edited by Chaudhuri, K., Jegelka, S., Song, L., Szepesvari, C., Niu, G., and Sabato, S., vol. 162 of *Proceedings of Machine Learning Research*, pp. 7919–7929, PMLR, 2022.

He, K., Zhang, X., Ren, S., and Sun, J.: Deep Residual Learning for Image Recognition, in: 2016 IEEE Conference on Computer Vision and
    Pattern Recognition (CVPR), pp. 770–778, https://doi.org/10.1109/CVPR.2016.90, 2016.

Hochreiter, S. and Schmidhuber, J.: Long Short-Term Memory, Neural Computation, 9, 1735–1780,
    https://doi.org/10.1162/neco.1997.9.8.1735, 1997.

Jin, F.-F., Boucharel, J., and Lin, I.-I.: Eastern pacific tropical cyclones intensified by el niño delivery of subsurface ocean heat, Nature, 516,
    82–85, https://doi.org/10.1038/nature13958, 2014.

Johnson, E. S., Bonjean, F., Lagerloef, G. S. E., Gunn, J. T., and Mitchum, G. T.: Validation and error analysis of OSCAR sea surface
    currents, Journal of Atmospheric and Oceanic Technology, 24, 688–701, https://doi.org/10.1175/JTECH1971.1, 2007.

Kukulka, T. and Harcourt, R. R.: Influence of stokes drift decay scale on langmuir turbulence, Journal of Physical Oceanography, 47, 1637–
    1656, https://doi.org/10.1175/JPO-D-16-0244.1, 2017.

Lagerloef, G. S. E., Mitchum, G. T., Lukas, R. B., and Niiler, P. P.: Tropical pacific near-surface currents estimated from altimeter, wind, and
    drifter data, Journal of Geophysical Research: Oceans, 104, 23 313–23 326, https://doi.org/10.1029/1999JC900197, 1999.

Lagerloef, G. S. E., Lukas, R., Bonjean, F., Gunn, J. T., Mitchum, G. T., Bourassa, M., and Busalacchi, A. J.: El Niño tropical pacific
    ocean surface current and temperature evolution in 2002 and outlook for early 2003, Geophysical Research Letters, 30, 2003GL017 096,
    https://doi.org/10.1029/2003GL017096, 2003.

Lam, R., Sanchez-Gonzalez, A., Willson, M., Wirnsberger, P., Fortunato, M., Alet, F., Ravuri, S., Ewalds, T., Eaton-Rosen, Z., Hu, W.,
    Merose, A., Hoyer, S., Holland, G., Vinyals, O., Stott, J., Pritzel, A., Mohamed, S., and Battaglia, P.: Learning skillful medium-range
    global weather forecasting, Science, 382, 1416–1421, https://doi.org/10.1126/science.adi2336, 2023.

Law-Chune, S., Aouf, L., Dalphinet, A., Levier, B., Drillet, Y., and Drevillon, M.: WAVERYS: a CMEMS global wave reanalysis during the
    altimetry period, Ocean Dynamics, 71, 357–378, https://doi.org/10.1007/s10236-020-01433-w, 2021.

LeCun, Y., Bengio, Y., and Hinton, G.: Deep learning, Nature, 521, 436–444, https://doi.org/10.1038/nature14539, 2015.

Liu, J., Emery, W. J., Wu, X., Li, M., Li, C., and Zhang, L.: Computing ocean surface currents from GOCI ocean color satellite imagery,
    IEEE Transactions on Geoscience and Remote Sensing, 55, 7113–7125, https://doi.org/10.1109/TGRS.2017.2741924, 2017.

Liu, Z., Mao, H., Wu, C.-Y., Feichtenhofer, C., Darrell, T., and Xie, S.: A ConvNet for the 2020s, in: 2022 IEEE/CVF Conference on
    Computer Vision and Pattern Recognition (CVPR), pp. 11 966–11 976, https://doi.org/10.1109/CVPR52688.2022.01167, 2022.

Lo, H. K. and McCord, M. R.: Adaptive ship routing through stochastic ocean currents: general formulations and empirical results, Trans-
    portation Research Part A: Policy and Practice, 32, 547–561, https://doi.org/10.1016/S0965-8564(98)00018-4, 1998.

Lyard, F., Lefevre, F., Letellier, T., and Francis, O.: Modelling the global ocean tides: modern insights from FES2004, Ocean Dynamics, 56,
    394–415, https://doi.org/10.1007/s10236-006-0086-x, 2006.

Niiler, P. P. and Paduan, J. D.: Wind-driven motions in the northeast pacific as measured by lagrangian drifters, Journal of Physical Oceanog-
    raphy, 25, 2819–2830, https://doi.org/10.1175/1520-0485(1995)025<2819:WDMITN>2.0.CO;2, 1995.

Oey, L., Ezer, T., Wang, D., Fan, S., and Yin, X.: Loop current warming by hurricane wilma, Geophysical Research Letters, 33,
    2006GL025 873, https://doi.org/10.1029/2006GL025873, 2006.

Onink, V., Wichmann, D., Delandmeter, P., and Van Sebille, E.: The role of ekman currents, geostrophy, and stokes drift in the accumulation
    of floating microplastic, Journal of Geophysical Research: Oceans, 124, 1474–1490, https://doi.org/10.1029/2018JC014547, 2019.

Pujol, M.-I., Faugère, Y., Taburet, G., Dupuy, S., Pelloquin, C., Ablain, M., and Picot, N.: DUACS DT2014: the new multi-mission altimeter
    data set reprocessed over 20years, Ocean Science, 12, 1067–1090, https://doi.org/10.5194/os-12-1067-2016, 2016.

Ricciardulli, L., Wentz, F., and Smith, D.: Remote Sensing Systems QuikSCAT Ku-2011 [Daily] Ocean Vector Winds on 0.25 deg grid, Version 4, www.remss.com/missions/qscat, 2011.

Rio, M., Mulet, S., and Picot, N.: Beyond GOCE for the ocean circulation estimate: synergetic use of altimetry, gravimetry, and in situ data provides new insight into geostrophic and ekman currents, Geophysical Research Letters, 41, 8918–8925, https://doi.org/10.1002/2014GL061773, 2014.

Rio, M.-H. and Santoleri, R.: Improved global surface currents from the merging of altimetry and sea surface temperature data, Remote Sensing of Environment, 216, 770–785, https://doi.org/10.1016/j.rse.2018.06.003, 2018.

Roach, C. J., Phillips, H. E., Bindoff, N. L., and Rintoul, S. R.: Detecting and characterizing ekman currents in the southern ocean, Journal of Physical Oceanography, 45, 1205–1223, https://doi.org/10.1175/JPO-D-14-0115.1, 2015.

Sudre, J. and Morrow, R. A.: Global surface currents: a high-resolution product for investigating ocean dynamics, Ocean Dynamics, 58, 101–118, https://doi.org/10.1007/s10236-008-0134-9, 2008.

Sudre, J., Maes, C., and Garçon, V.: On the global estimates of geostrophic and ekman surface currents, Limnology and Oceanography: Fluids and Environments, 3, 1–20, https://doi.org/10.1215/21573689-2071927, 2013.

Sun, W., Zhou, X., Zhou, D., and Sun, Y.: Advances and accuracy assessment of ocean tide models in the antarctic ocean, Frontiers in Earth Science, 10, 757 821, https://doi.org/10.3389/feart.2022.757821, 2022.

Taguchi, E., Stammer, D., and Zahel, W.: Inferring deep ocean tidal energy dissipation from the global high-resolution data-assimilative HAMTIDE model, Journal of Geophysical Research: Oceans, 119, 4573–4592, https://doi.org/10.1002/2013JC009766, 2014.

Van Meurs, P. and Niiler, P. P.: Temporal variability of the large-scale geostrophic surface velocity in the northeast pacific*, Journal of Physical Oceanography, 27, 2288–2297, https://doi.org/10.1175/1520-0485(1997)027<2288:TVOTLS>2.0.CO;2, 1997.

Vaswani, A., Shazeer, N., Parmar, N., Uszkoreit, J., Jones, L., Gomez, A. N., Kaiser, L., and Polosukhin, I.: Attention is All You Need, in: Proceedings of the 31st International Conference on Neural Information Processing Systems, NIPS'17, p. 6000–6010, Curran Associates Inc., Red Hook, NY, USA, ISBN 9781510860964, 2017.

Wahl, T., Skøelv, A., Pedersen, J. P., Seljelv, L., Andersen, J. H., Follum, O. A., Anderssen, T., Strøm, G. D., Bern, T., Espedal, H. H., Hamnes, H., and Solberg, R.: Radar satellites: a new tool for pollution monitoring in coastal waters, Coastal Management, 24, 61–71, https://doi.org/10.1080/08920759609362281, 1996.

Weisberg, R. H., Liu, Y., Lembke, C., Hu, C., Hubbard, K., and Garrett, M.: The coastal ocean circulation influence on the 2018 west florida shelf *K. brevis* red tide bloom, Journal of Geophysical Research: Oceans, 124, 2501–2512, https://doi.org/10.1029/2018JC014887, 2019.

Wentz, F., Ricciardulli, L., Gentemann, C., Meissner, T., Hilburn, K., and Scott, J.: Remote Se-nsing Systems Coriolis WindSat [Daily] Environmental Suite on 0.25 deg grid, Version 7.0.1, www.remss.com/missions/windsat, 2013.

Yang, H., Choi, J., Park, Y., Han, H., and Ryu, J.: Application of the geostationary ocean color imager (GOCI) to estimates of ocean surface currents, Journal of Geophysical Research: Oceans, 119, 3988–4000, https://doi.org/10.1002/2014JC009981, 2014.